Multi-parameter inversion with the aid of particle velocity field reconstruction

Taskin, Ulas; Van Dongen, Koen W.A.

DOI
10.1121/10.0001396

Publication date
2020

Document Version
Accepted author manuscript

Published in
Journal of the Acoustical Society of America

Multi-parameter inversion with the aid of particle velocity field reconstruction

Ulas Taskin[1, a)] and Koen W. A. van Dongen[1]

Department of Imaging Physics, Delft University of Technology, Delft, 2628CJ, the Netherlands.

(Dated: 27 July 2020)

Multi-parameter inversion for medical ultrasound leads to an improved tissue classification. In general, simultaneous reconstruction of volume density of mass and compressibility would require knowledge of the particle velocity field alongside with the pressure field. However, in practice the particle velocity field is not measured. Here, we propose a method for multi-parameter inversion where the particle velocity field is reconstructed from the measured pressure field. To this end, the measured pressure field is described using outward propagating Hankel functions. For a synthetic setup, it is shown that the reconstructed particle velocity field matches the forward modelled particle velocity field. Next, the reconstructed particle velocity field is used together with the synthetically measured pressure field to reconstruct density and compressibility profiles with the aid of contrast source inversion (CSI). Finally, comparing the reconstructed speed of sound profiles obtained via single-parameter versus multi-parameter inversion shows that multi-parameter outperforms single-parameter inversion with respect to accuracy and stability.

[a)] u.taskin@tudelft.nl; Department of Imaging Physics, Delft University of Technology, Delft, 2628CJ, the Netherlands.

I. INTRODUCTION

Ultrasound is widely used as a medical imaging modality due to its features such as being non-invasive and safe. To retrieve quantitative information about the tissues in the image, ultrasound tomography[1–3] in combination with full-wave inversion[4–7] is frequently used. Up to date, these methods are successfully applied in cases where the object is surrounded by transducers. Examples are the breast[8], brain[9] and bone[10].

Most inversion methods aim for speed of sound reconstruction by assuming constant mass density. This is mainly done to simplify the complex non-linear inverse problem. However, quantitative knowledge about multiple medium parameters may lead to an improved tissue characterization[11].

In various recent works, full-wave inversion is used for multi-parameter reconstruction. For example, contrast source inversion (CSI) and Born iterative method (BIM) are used to reconstruct compressibility, attenuation and density[12,13]. In these works the parameters are directly reconstructed from the pressure field measurements. However, with these methods additional regularization is needed to reconstruct the density accurately[14]. Alternatively, the particle velocity field is used together with the pressure field to reconstruct density and compressibility simultaneously using a full vectorial CSI scheme[15]. Unfortunately, in practice only the pressure field is measured and the particle velocity field is unknown. Therefore, full vectorial CSI method can not be used directly in practical applications.

In this work, we propose a multi-parameter inversion method where we first reconstruct the particle velocity field from the pressure field measured on a closed arbitrary-shaped

two-dimensional (2-D) curvature. The particle velocity field reconstruction method is based on Hankel function decomposition of the measured pressure field[16]. Once the pressure field is expressed with Hankel functions, the particle velocity field is computed by applying the gradient operator to the derived expression. After a successful reconstruction of the particle velocity field from the pressure field, both the compressibility and the mass density are reconstructed using a vectorial CSI scheme[15].

The paper is organized as follows: Section II presents the forward model, the method to reconstruct the particle velocity field from the pressure field and finally the inverse problem. Section III presents numerical examples in which the reconstructed particle velocity field is compared with the ground truth. In addition, reconstructed density, compressibility and speed of sound profiles are presented. These profiles are obtained by employing CSI on the measured pressure and reconstructed particle velocity field. Finally, conclusions are given in Section IV.

II. THEORY

Consider an arbitrary-shaped object with unknown medium properties within the spatial domain $\mathbb{D}$ enclosed by the boundary $\mathbb{S}$. The sources and receivers are located on the boundary $\mathbb{S}$, see Fig. 1. The boundary $\mathbb{S}$ is located in the homogeneous lossless embedding with speed of sound c_0, volume density of mass ρ_0 and compressibility κ_0. The object domain is heterogeneous in all three medium parameters. The Cartesian and polar position vectors are denoted by $\boldsymbol{x} = (x, y)$ and $\boldsymbol{r} = (r, \phi)$ respectively. The following theory is presented in the temporal Fourier domain with angular frequency ω.

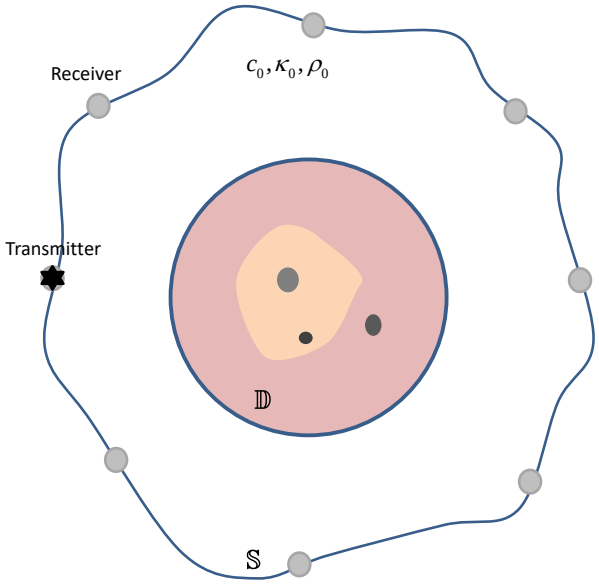

FIG. 1. Schematic representation of the setup. Transmitters and receivers are located in $\mathbb{S}$. $\mathbb{S}$ encloses the object within the domain $\mathbb{D}$.

A. Forward Problem

The acoustic field equations are given by the equation of motion and deformation. In the temporal Fourier domain these equations read[17,18]

$$\nabla \hat{p}(\boldsymbol{x}) + j\omega\rho(\boldsymbol{x})\hat{\boldsymbol{v}}(\boldsymbol{x}) = \hat{\boldsymbol{f}}(\boldsymbol{x}) \tag{1}$$

and

$$\nabla \cdot \hat{\boldsymbol{v}}(\boldsymbol{x}) + j\omega\kappa(\boldsymbol{x})\hat{p}(\boldsymbol{x}) = \hat{q}(\boldsymbol{x}), \tag{2}$$

where $\hat{p}(\boldsymbol{x})$ is the pressure wave field, $\hat{\boldsymbol{v}}(\boldsymbol{x})$ is the particle velocity wave field, $\rho(\boldsymbol{x})$ is the volume density of mass, $\kappa(\boldsymbol{x})$ is the compressibility, $\hat{\boldsymbol{f}}(\boldsymbol{x})$ is the volume source density of volume force, $\hat{q}(\boldsymbol{x})$ is the volume source density of injection rate, j is the imaginary number defined via the relation $j^2 = -1$, and ∇ is the nabla operator. The caret symbol $\hat{}$ is used

for quantities defined in the temporal Fourier domain. The incident wave fields $\hat{p}^{inc}(\boldsymbol{x})$ and $\hat{\boldsymbol{v}}^{inc}(\boldsymbol{x})$ are defined as the wave fields that are generated by the primary sources $\hat{q}(\boldsymbol{x})$ and $\hat{\boldsymbol{f}}(\boldsymbol{x})$, and that propagate in the homogeneous embedding in the absence of any acoustic contrast. In view of this definition, the scattered wave fields $\hat{p}^{sct}(\boldsymbol{x})$ and $\hat{\boldsymbol{v}}^{sct}(\boldsymbol{x})$ are defined as the numerical difference between the actual or total wave fields $\hat{p}(\boldsymbol{x})$ and $\hat{\boldsymbol{v}}(\boldsymbol{x})$, and the incident wave fields $\hat{p}^{inc}(\boldsymbol{x})$ and $\hat{\boldsymbol{v}}^{inc}(\boldsymbol{x})$. The scattered fields can be written in integral form as[17,18]

$$\begin{aligned}\hat{p}^{sct}(\boldsymbol{x}) = \hat{p}(\boldsymbol{x}) - \hat{p}^{inc}(\boldsymbol{x}) =& \frac{\omega^2}{c_0^2}\int_{\boldsymbol{x}'\in\mathbb{D}} \hat{G}(\boldsymbol{x}-\boldsymbol{x}')\chi^{\kappa}(\boldsymbol{x}')\hat{p}(\boldsymbol{x}')\mathrm{d}V(\boldsymbol{x}') \\ &+ j\omega\rho_0\nabla\cdot\int_{\boldsymbol{x}'\in\mathbb{D}} \hat{G}(\boldsymbol{x}-\boldsymbol{x}')\chi^{\rho}(\boldsymbol{x}')\hat{\boldsymbol{v}}(\boldsymbol{x}')\mathrm{d}V(\boldsymbol{x}')\end{aligned} \tag{3}$$

and

$$\begin{aligned}\hat{\boldsymbol{v}}^{sct}(\boldsymbol{x}) = \hat{\boldsymbol{v}}(\boldsymbol{x}) - \hat{\boldsymbol{v}}^{inc}(\boldsymbol{x}) =& j\omega\kappa_0\nabla\int_{\boldsymbol{x}'\in\mathbb{D}} \hat{G}(\boldsymbol{x}-\boldsymbol{x}')\chi^{\kappa}(\boldsymbol{x}')\hat{p}(\boldsymbol{x}')\mathrm{d}V(\boldsymbol{x}') \\ &- \nabla\nabla\cdot\int_{\boldsymbol{x}'\in\mathbb{D}} \hat{G}(\boldsymbol{x}-\boldsymbol{x}')\chi^{\rho}(\boldsymbol{x}')\hat{\boldsymbol{v}}(\boldsymbol{x}')\mathrm{d}V(\boldsymbol{x}') - \chi^{\rho}(\boldsymbol{x})\hat{\boldsymbol{v}}(\boldsymbol{x}),\end{aligned} \tag{4}$$

where $\hat{G}(\boldsymbol{x}-\boldsymbol{x}')$ is the Green's function describing the impulse response of the homogeneous embedding. The Green's function in 2-D equals

$$\hat{G}(\boldsymbol{x}-\boldsymbol{x}') = \frac{i}{4}H_0^{(1)}(k_0|\boldsymbol{x}-\boldsymbol{x}'|) \tag{5}$$

where $H_0^{(1)}$ is the zero-order Hankel function of the first kind. The contrast functions $\boldsymbol{\chi}^{\kappa}(\boldsymbol{x})$ and $\boldsymbol{\chi}^{\rho}(\boldsymbol{x})$ are defined as

$$\boldsymbol{\chi}^{\kappa}(\boldsymbol{x}) = \frac{\kappa(\boldsymbol{x})-\kappa_0}{\kappa_0} \tag{6}$$

and

$$\boldsymbol{\chi}^{\rho}(\boldsymbol{x}) = \frac{\rho(\boldsymbol{x})-\rho_0}{\rho_0}. \tag{7}$$

Eqs. (3) and (4) can be solved numerically for known sources and known contrast functions to find the unknown total wave fields inside the spatial domain $\mathbb{D}$. In literature, this situation is referred to as the forward problem. The situation where the sources generating the wave fields as well as the total wave fields at the boundary $\mathbb{S}$ are known, and where both the total wave fields and the contrast functions are unknown within the domain of interest $\mathbb{D}$ is referred to as the inverse problem. Unfortunately, in practice one only measures the pressure field and not the particle velocity field. In the next section we present a method that allows us to reconstruct the particle velocity field from the measured pressure field.

B. particle Velocity Field Reconstruction

Multi-parameter inversion requires knowledge of both the pressure and particle velocity wave fields, where the latter one is not measured in practice. Here we present a method to construct the particle velocity field from pressure field measurements.

The scattered field satisfies the 2-D Helmholtz equation, which reads in polar coordinates

$$r^2\frac{\partial^2\hat{p}^{sct}\left(\boldsymbol{r}\right)}{\partial r^2}+r\frac{\partial\hat{p}^{sct}\left(\boldsymbol{r}\right)}{\partial r}+\frac{\partial^2\hat{p}^{sct}\left(\boldsymbol{r}\right)}{\partial\phi^2}+r^2\frac{\omega^2}{c^2(\boldsymbol{r})}\hat{p}^{sct}\left(\boldsymbol{r}\right)=0. \tag{8}$$

Under the condition that the solution of Eq. (8) represents an outward propagating wave field at the boundary of $\mathbb{S}$, the resulting scattered field may be formulated as[16]

$$\hat{p}^{sct}\left(\boldsymbol{r}\right)=\sum_{n=-N}^{N}\hat{c}_nH_n^{(1)}\left(\frac{\omega}{c_0}r\right)e^{jn\phi}, \tag{9}$$

where $H_n^{(1)}\left(\frac{\omega}{c_0}r\right)$ are Hankel functions of the first kind and order n representing the outward propagating waves[19]. To find the complex valued coefficients $\hat{c}_n$ for each angular frequency

ω, Eq. (9) is solved for $\hat{c}_n$ using the known scattered pressure field $\hat{p}^{sct}(\boldsymbol{r})$ measured on $\mathbb{S}$[16]. Once the coefficients $\hat{c}_n$ are reconstructed, the scattered particle velocity field $\hat{\boldsymbol{v}}^{sct}(\mathbf{r})$ is computed by considering the gradient of the scattered pressure field, hence

$$\hat{\boldsymbol{v}}^{sct}(\mathbf{r}) = -\frac{1}{j\omega\rho_0}\nabla\hat{p}^{sct}(\mathbf{r}). \tag{10}$$

By combining Eqs. (9) and (10) the following expressions for the particle velocity field in cylindrical coordinates $\hat{\boldsymbol{v}}^{sct}(\boldsymbol{r}) = (\hat{v_r}^{sct}(\boldsymbol{r}), \hat{v_\phi}^{sct}(\boldsymbol{r}))$ are obtained

$$\begin{aligned}\hat{v}_r^{sct}(\mathbf{r}) &= -\frac{1}{j\omega\rho_0}\frac{\partial\hat{p}^{sct}(\boldsymbol{r})}{\partial r} \\ &= -\frac{1}{j\omega\rho_0}\times\sum_{n=-N}^{N}\left[H_{n-1}^{(1)}\left(\frac{\omega}{c_0}r\right) - H_{n+1}^{(1)}\left(\frac{\omega}{c_0}r\right)\right]\hat{c}_n\frac{\omega}{2c_0}e^{jn\phi}\end{aligned} \tag{11}$$

and

$$\hat{v}_\phi^{sct}(\mathbf{r}) = -\frac{1}{j\omega\rho_0}\frac{\partial\hat{p}^{sct}(\boldsymbol{r})}{\partial\phi} = -\frac{1}{j\omega\rho_0}\times\sum_{n=-N}^{N} jn\hat{c}_n H_n^{(1)}\left(\frac{\omega}{c_0}r\right)e^{jn\phi}, \tag{12}$$

where we use recurrence relations to compute the spatial derivatives of the Hankel functions[20].

C. Inverse Problem

Full-wave inversion methods aim to reconstruct medium parameters by iteratively minimizing a cost function. Typically, this cost function contains at least one term that shows a measure for the mismatch between the measured and the modelled wave fields. A well-known full-wave inversion method is CSI. This method can be implemented such that it reconstructs multiple medium parameters simultaneously[15].

1. *Multi-parameter inversion*

Employing CSI for a multi-parameter inverse problem requires the formulation of the following cost functional

$$\mathrm{Err}^{(1)} = \eta_{\mathbb{S}}^{pv} \left\| \begin{matrix} \mathbf{p}^{sct} - \mathbf{L}_p^{\mathbb{S}}[\mathbf{w}^{\kappa}, \mathbf{w}^{\rho}] \\ \mathbf{v}^{sct} - \mathbf{L}_v^{\mathbb{S}}[\mathbf{w}^{\kappa}, \mathbf{w}^{\rho}] \end{matrix} \right\|_{\mathbb{S}}^2 + \eta_{\mathbb{D}}^{pv} \left\| \begin{matrix} \boldsymbol{\chi}^{\kappa}\mathbf{p}^{inc} + \boldsymbol{\chi}^{\kappa}\mathbf{L}_p^{\mathbb{D}}[\mathbf{w}^{\kappa}, \mathbf{w}^{\rho}] - \mathbf{w}^{\kappa} \\ \boldsymbol{\chi}^{\rho}\mathbf{v}^{inc} + \boldsymbol{\chi}^{\rho}\mathbf{L}_v^{\mathbb{D}}[\mathbf{w}^{\kappa}, \mathbf{w}^{\rho}] - \mathbf{w}^{\rho} \end{matrix} \right\|_{\mathbb{D}}^2, \tag{13}$$

where $\eta_{\mathbb{S}}^{pv}$ and $\eta_{\mathbb{D}}^{pv}$ are normalization terms, $\mathbf{L}_p^{\mathbb{S}}$, $\mathbf{L}_p^{\mathbb{D}}$, $\mathbf{L}_v^{\mathbb{S}}$ and $\mathbf{L}_v^{\mathbb{D}}$ are integral operators that map the contrast sources $\mathbf{w}^{\kappa}$ and $\mathbf{w}^{\rho}$ to the pressure and particle velocity wave fields in $\mathbb{S}$ and $\mathbb{D}$, and where $||\cdot||_{\mathbb{S}}$ and $||\cdot||_{\mathbb{D}}$ represent the l_2-norm of a quantity defined in $\mathbb{S}$ and $\mathbb{D}$ respectively. For a spatially varying compressibility and density the contrast sources equal

$$\mathbf{w}^{\kappa} = \chi^{\kappa}\mathbf{p} \tag{14}$$

and

$$\mathbf{w}^{\rho} = \chi^{\rho}\mathbf{v}. \tag{15}$$

To solve the inverse problem for the unknown contrast functions χ^{κ} and χ^{ρ}, the cost function in Eq. (13) is minimized iteratively for known incident fields in $\mathbb{S}$ and $\mathbb{D}$ and scattered fields in $\mathbb{S}$.

2. *Single-parameter inversion*

It is common practice to assume a constant density throughout the entire domain, i.e. $\rho(\boldsymbol{r}) = \rho_0$. Within this assumption the vectorial problem reduces to a scalar problem and

the cost function $\mathrm{Err}^{(1)}$ for CSI that needs to be minimized reduces to,[21]

$$\mathrm{Err}^{(2)} = \eta_{\mathbb{S}} \left\| \mathbf{p}^{\mathrm{sct}} - \mathbf{L}_p^{\mathbb{S}}[\mathbf{w}^{\kappa}] \right\|_{\mathbb{S}}^2 + \eta_{\mathbb{D}} \left\| \boldsymbol{\chi}^{\kappa} \mathbf{p}^{\mathrm{inc}} - \mathbf{w}^{\kappa} - \boldsymbol{\chi}^{\kappa} \mathbf{L}_p^{\mathbb{D}}[\mathbf{w}^{\kappa}] \right\|_{\mathbb{D}}^2 . \tag{16}$$

Note that, for this single-parameter inversion a spatially varying speed of sound profile is obtained via the relation $c(\boldsymbol{x}) = \frac{1}{\sqrt{\kappa(\boldsymbol{x})\rho_0}}$.

III. RESULTS

A synthetic example is presented in this section. First, the forward problem is solved to obtain both pressure and particle velocity fields[22]. Next, the particle velocity field is computed with the proposed method and compared with the "exact" result obtained by directly solving the forward problem. Finally, contrasts source inversion (CSI) is used as a multi- and single-parameter inversion method.

A. Configuration

A synthetic "breast" phantom is used in this work. The phantom alongside with the transducer locations is shown in Fig. 2. The medium parameters of the tissues are listed in Table I[23,24]. Attenuation is neglected since it is known to have little effect on the acoustic fields at these frequencies[25]. The spatial domain contains 100×100 elements of size $0.42\ \mathrm{mm} \times 0.42\ \mathrm{mm}$. The 32 sources and 128 receivers are equally distributed over the white dotted circle indicating $\mathbb{S}$ (see Fig. 2)[26]. In Fig. 3, the source excitation is given; a Gaussian modulated pulse with a center frequency $f_0 = 0.2$ MHz.

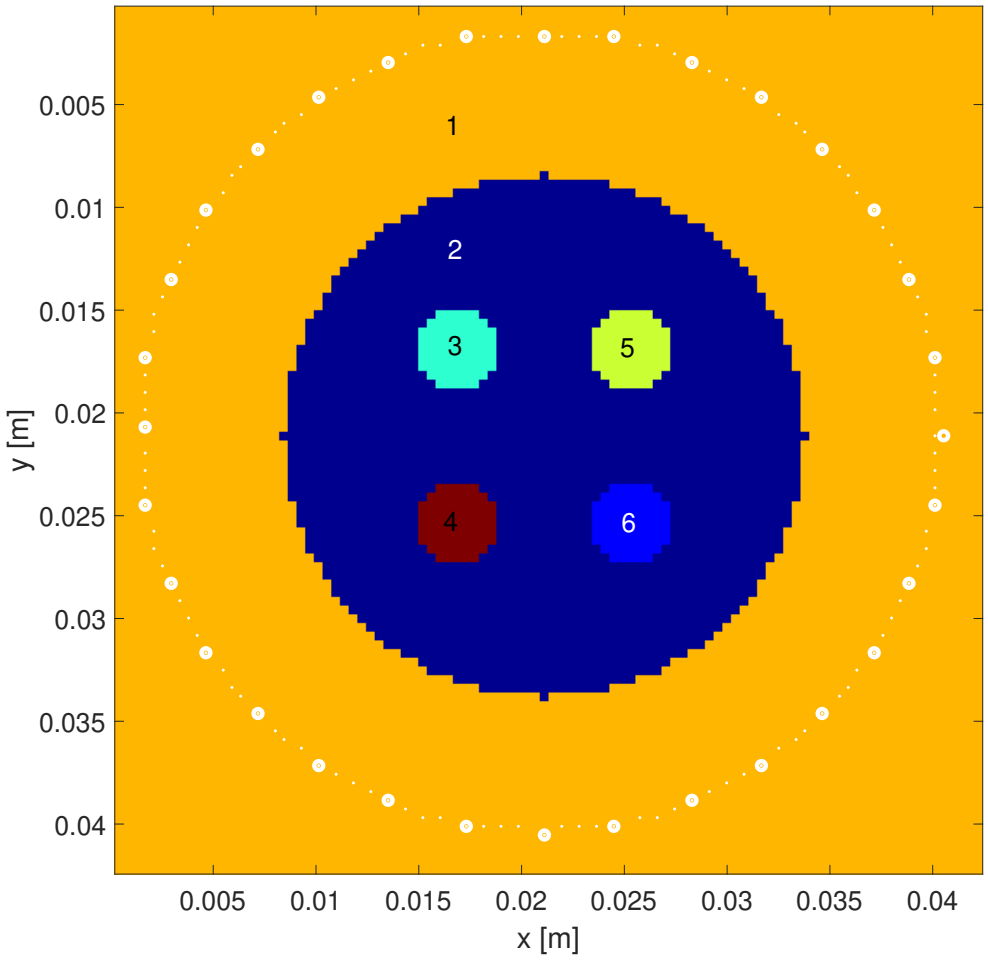

FIG. 2. Synthetic breast phantom. The large and small white dots show the locations of the sources and the receivers respectively. The numbers indicate the different tissue types.

B. Solution of Forward Problem

Synthetic data (both pressure and particle velocity field) is obtained by solving the forward problem for the breast phantom in the frequency domain[22]. Time-domain results are obtained using inverse Fourier transformations.

Fig. 4 shows snapshots of the incident, scattered and total pressure and particle velocity fields at $t = 28$ μs. The source is located at $(x, y) = (21\text{ mm}, 41\text{ mm})$. The wave fields are

TABLE I. Medium parameters of the tissues.

Tissue #	c [m/s]	ρ [kg/m^3]	κ [1/Pa]
1	1520	996	0.435e-9
2	1494	1013	0.442e-9
3	1514	986	0.442e-9
4	1527	986	0.435e-9
5	1514	1013	0.430e-9
6	1494	1041	0.430e-9

computed by solving the full-wave forward problem for the pressure and particle velocity field simultaneously. The obtained particle velocity field will serve as a benchmark for the reconstructed particle velocity field.

C. particle Velocity Field Reconstruction

The particle velocity fields are reconstructed from the pressure fields using the proposed method. These pressure fields are synthetically measured by the 128 receivers indicated by the small white dots in Fig. 2 and a single source that is located at $(x, y) = (41\text{ mm}, 21\text{ mm})$.

First, frequency-domain results are shown in Fig. 5. The top row shows the pressure fields measured in the receiver locations; in blue the synthetically generated and in red the reconstructed pressure fields. The following rows show the particle velocity fields. It

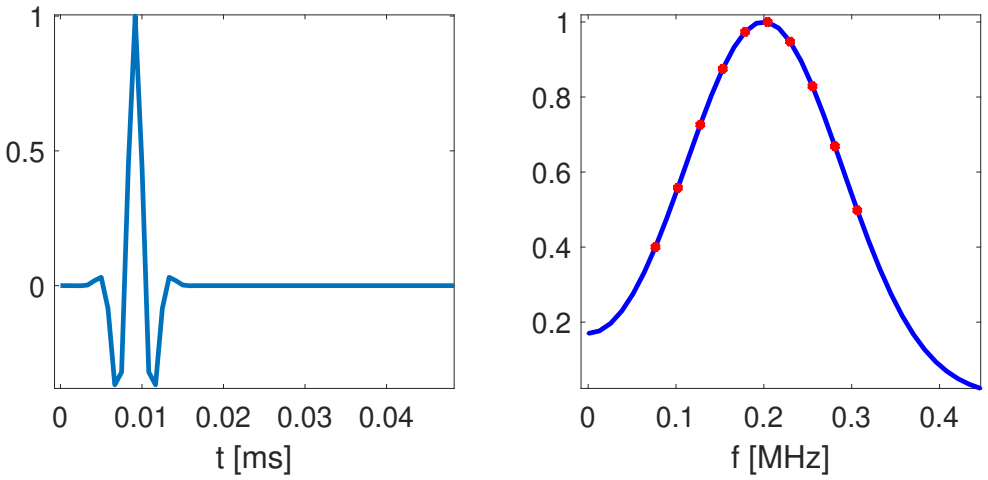

FIG. 3. Excitation profile in time (left) and frequency (right) domain. Red dots indicate the frequency components used with CSI.

is seen from these results that the reconstructed fields have an excellent match with the synthetically generated fields for both amplitude and phase.

Next, time-domain results are shown in Fig. 6. The source and receiver locations are given in the image at the top. A-scans at the given receiver locations for the particle velocity field are given in the bottom images. Ground truth and reconstructed fields are plotted together. These results show that the proposed method works well over the entire bandwidth.

D. Solution of Inverse Problem

The effect of the particle velocity field on the inversion is shown in this subsection. First, contrast source inversion (CSI) is used in its traditional way[27] by using only the pressure field and inverting for the speed of sound (assuming constant density) only. Note that, the forward problem is based on a spatially varying compressibility as well as density profile. Next, CSI is used as described in Ref. 15 by using pressure and particle velocity fields

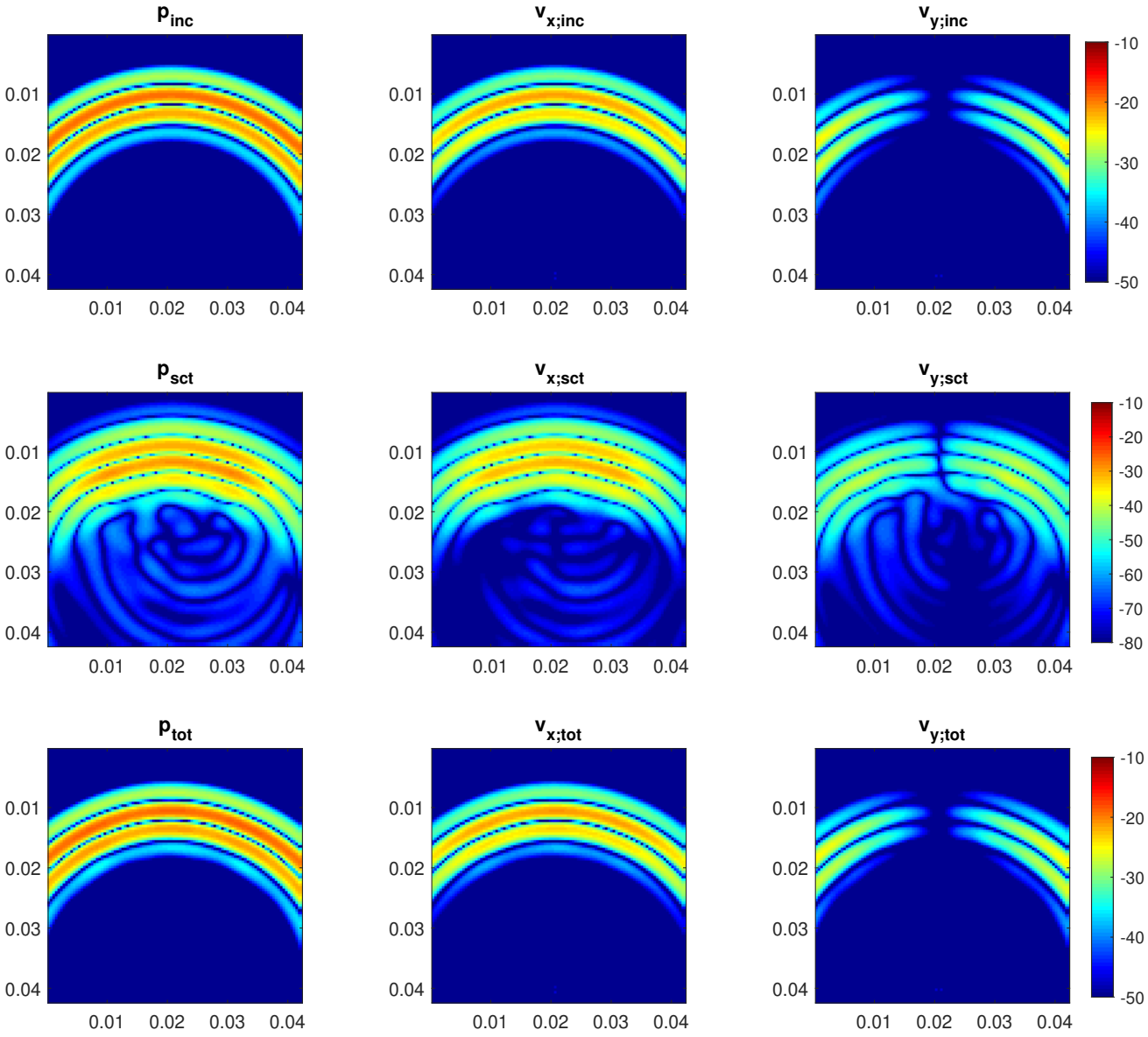

FIG. 4. Snapshots of incident (top row), scattered (middle row) and total fields (bottom row) at $t = 28\mu$s. Left column shows the pressure field; the middle and right columns the particle velocity fields. All fields are normalized with respect to the maximum absolute value and shown on a dB scale.

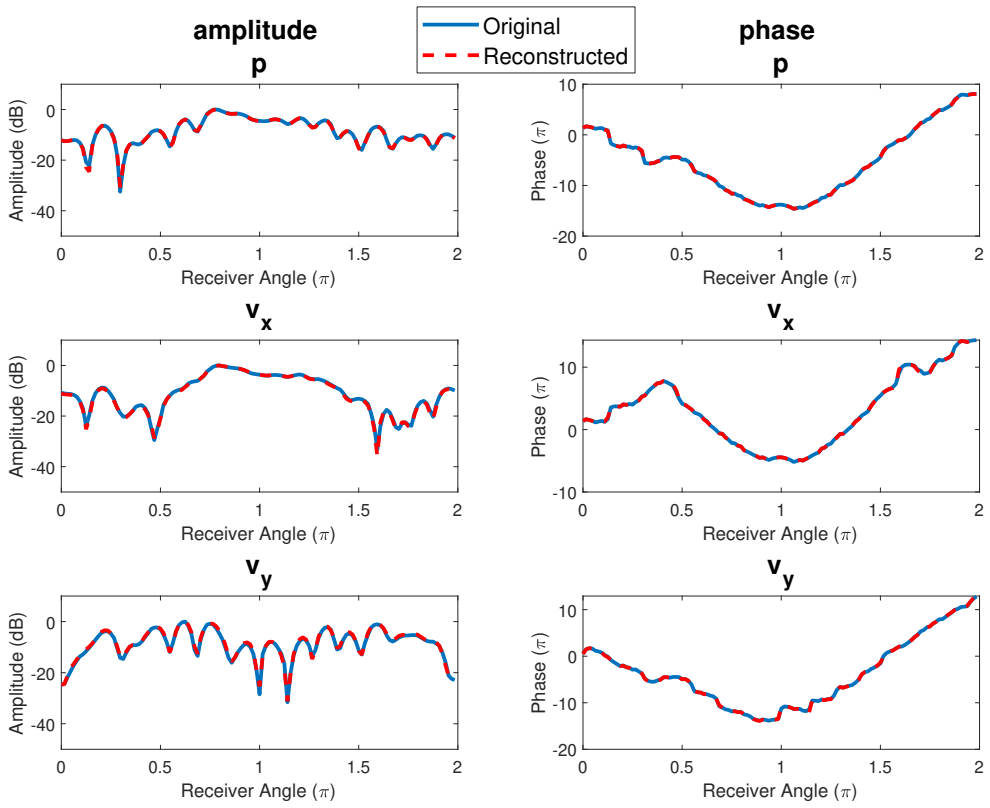

FIG. 5. particle velocity field reconstruction results in frequency domain. Both amplitude (left column) and phase (right column) of the synthetically generated and reconstructed fields are shown. Top row shows the Hankel decomposition of the pressure field (red) with the synthetically generated (blue); middle and bottom row the reconstructed particle velocity fields (red) together with the synthetically generated (blue).

together and inverting for both compressibility and density. For all examples, 32 sources and 128 receivers are used, all equally distributed on a circle with radius $r = 20$ mm, see Fig. 2. Ten frequency components are used for the inversion, see Fig. 3.

Fig. 7 shows the single-parameter inversion results obtained with CSI after 2048 iterations. The first row shows the true compressibility, density and speed of sound profiles. The second row shows the inversion results using pressure field only and assuming constant density.

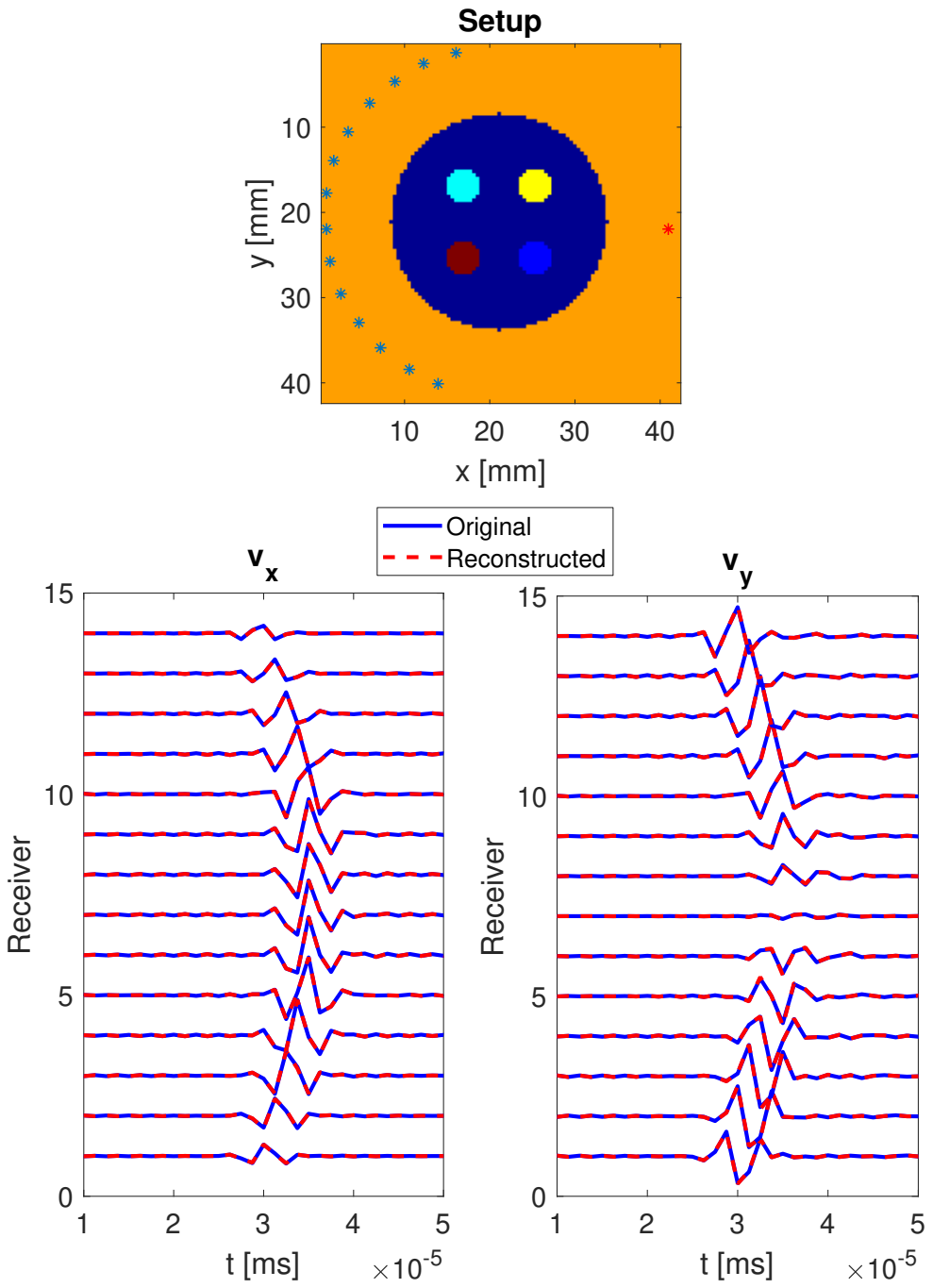

FIG. 6. particle velocity field reconstruction results in time domain. The top image shows the locations of the source (red star) and the 15 receivers (blue stars). The bottom images show the reconstructed particle velocity field (red) together with the ground truth (blue). Note that, all fields are normalized with respect to the maximum value.

The four small lesions are all visible in the results but with wrong parameter values. The values for the compressibility and density contrast in the lower right corner are selected such that small cylinder doesn't show any speed of sound contrast with respect to its direct surrounding but that it still will give rise to scattering. Not allowing for a density contrast during reconstruction automatically means the formation of an erroneous speed of sound contrast at this particular location.

Note that in literature there are works that show that single-parameter inversion reconstructs speed of sound accurately with experimental data. With this specific example we intended to show where these single-parameter inversion methods might face problems.

Fig. 8 shows the multi-parameter inversion results obtained with CSI after 2048 iterations. The first row shows the true compressibility, density and speed of sound profiles. These profiles are identical to the ones used in Fig. 7. The second row shows the inversion results using the synthetically generated pressure and particle velocity fields. The third row shows the inversion results when the synthetically generated pressure and reconstructed particle velocity fields are used to invert for both density and compressibility. In both cases similar results are obtained and the four small lesions have almost the correct parameter values. The ripples seen in the background are caused by the coarse discretization of the domain and can be solved by using a finer spatial discretization or additional regularization based on total variation or sparsity constraints[21,28]. Integral equation formulations have the advantage that they perform well with relatively coarse sampling because of having a bounded operator. This is valid for CSI for the single-parameter inversion. However, this feature is not valid for the multi-parameter inversion anymore. The operator in multi-parameter inversion is

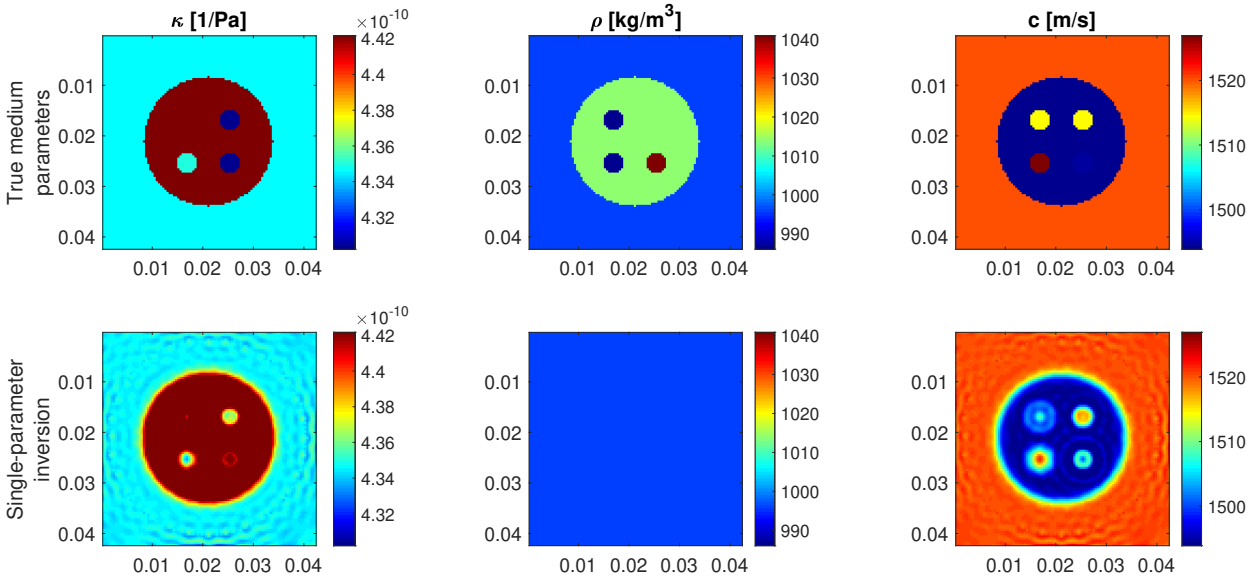

FIG. 7. Contrast source inversion results (single-parameter). Top row shows the true compressibility, density and speed of sound profiles; bottom row shows the CSI reconstruction using the synthetically generated pressure field only and assuming constant density. Note that with this example we intend to show the leakage of density contrast into a compressibility and hence speed of sound contrast.

unbounded because of the spatial derivatives. Therefore, a finer discretization would also improve these results.

To examine the performance of the method against noise, we added 5% complex valued white noise to the data. Results for the reconstructions are shown in Fig. 9. It can be seen from these results that all small inclusions are reconstructed with a good accuracy.

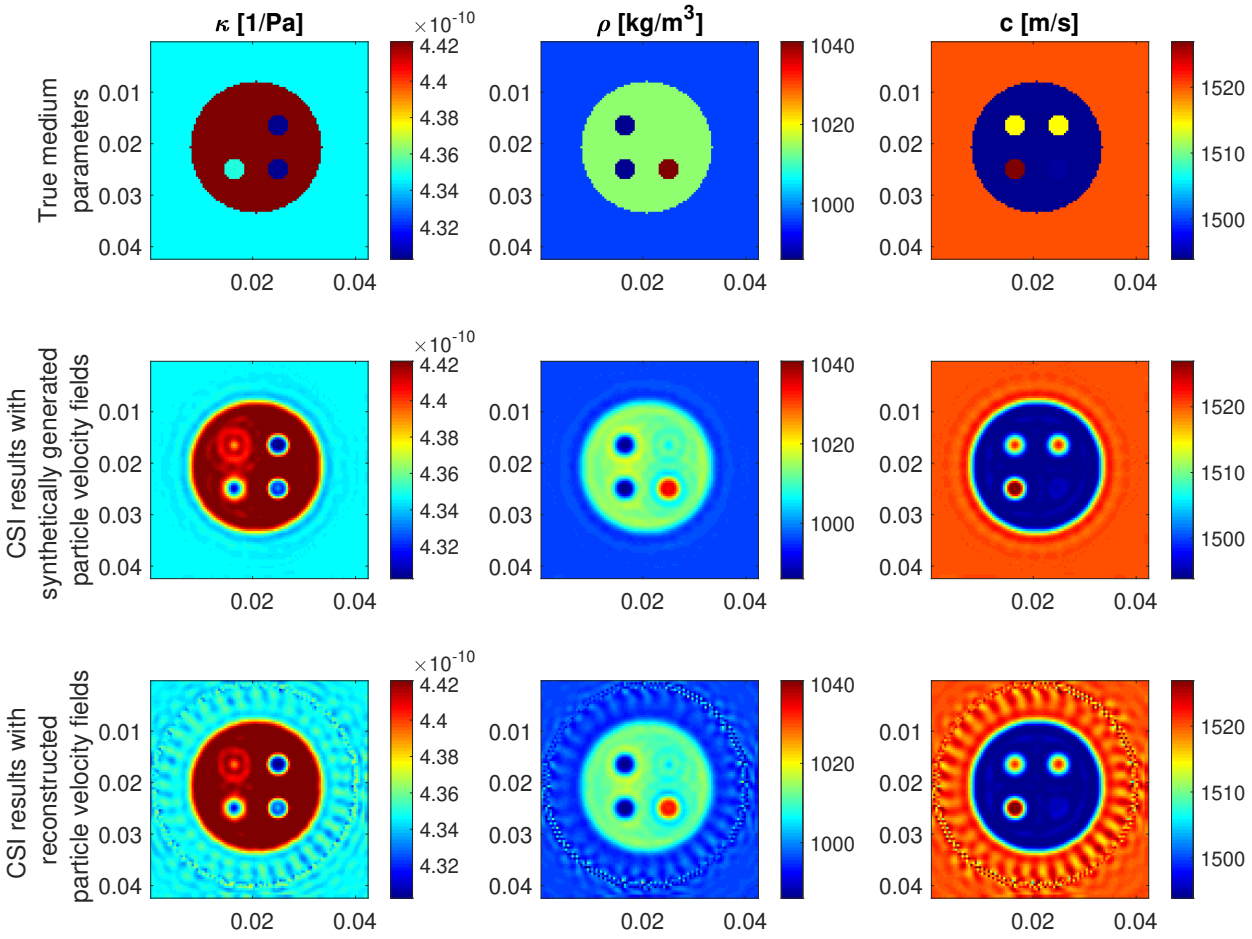

FIG. 8. Contrast source inversion results (multi-parameter). Top row shows the true compressibility, density and speed of sound profiles; middle row shows the CSI reconstruction using synthetically generated pressure and particle velocity fields; bottom row shows the CSI reconstruction using pressure field together with reconstructed particle velocity fields.

IV. CONCLUSION

In this paper, we present a multi-parameter full-wave inversion method where the required particle velocity field is reconstructed from the measured pressure field using Hankel function decomposition. The inversion method has been successfully tested using a 2-D synthetic

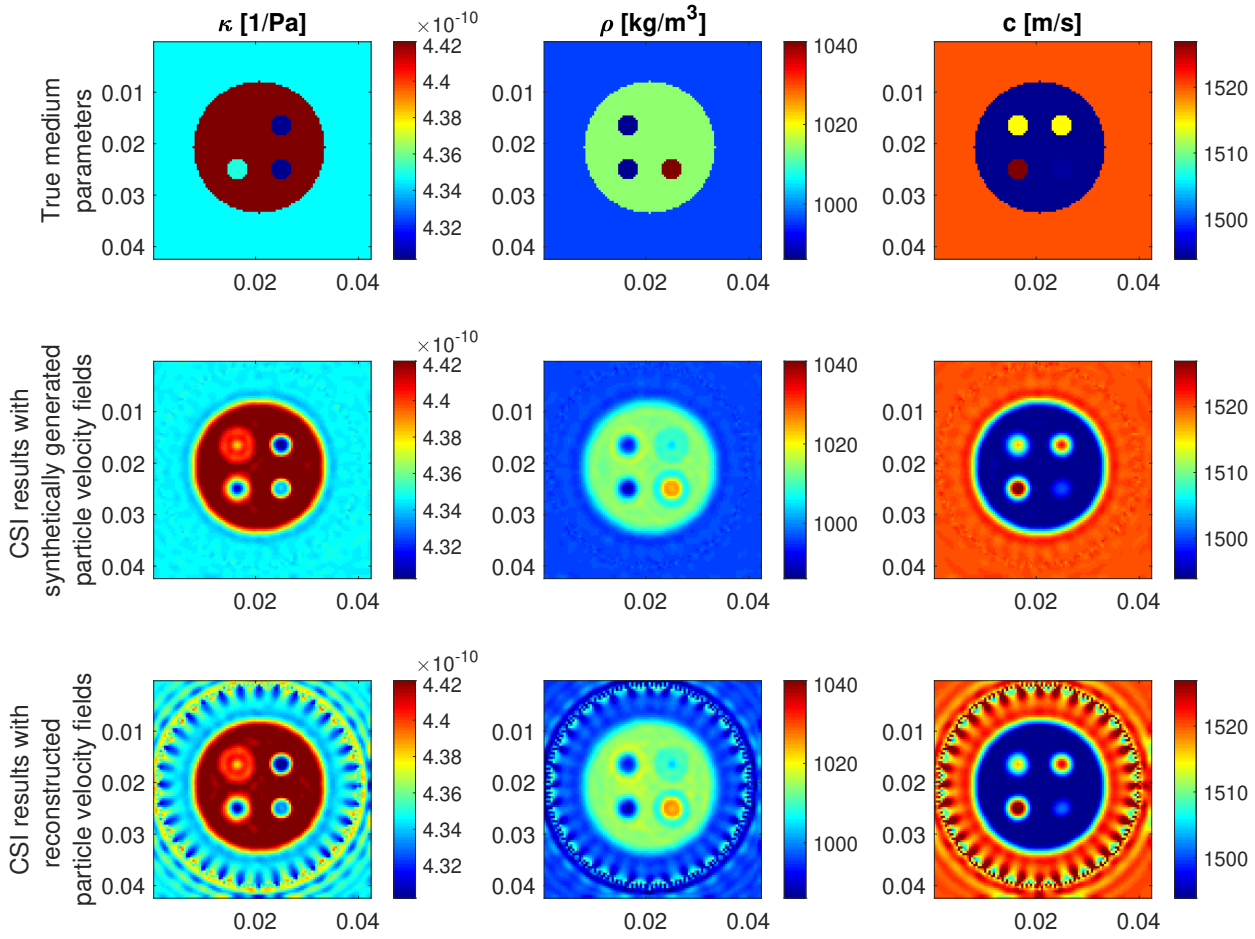

FIG. 9. Same as Fig. 8 but now with 5% noise added to the data.

example; a breast phantom containing heterogeneities in compressibility, density and speed of sound.

First we have tested the particle velocity field reconstruction method. To this end, the particle velocity field obtained by solving the full vectorial forward problem has been compared with the reconstructed particle velocity field using the synthetically measured pressure field. It has been shown that both particle velocity fields matches each other perfectly well.

Next, the synthetically measured pressured field has been used together with the reconstructed particle velocity field to successfully invert for density, compressibility and speed-of

sound profiles using a full-wave inversion method referred to as contrast source inversion (CSI). Finally, CSI has been implemented in its traditional way where only a pressure field is used to invert for a speed of sound profile given the assumption of a constant density. Application of this single-parameter inversion on the synthetic data derived from the multi-parameter synthetic breast phantom gives rise to "ghost" objects in the resulting speed of sound profile. These results underline the importance of multi-parameter inversion in case the object of interest shows spatial variations in compressibility, density and speed of sound.

Attenuation is another important parameter in medical ultrasound. There are already quite some inversion related work that includes attenuation. We believe that it needs detailed examination in a future paper. Finally, a 3-D extension of the method introduced in this paper is straightforward and would only lead to an increase in computational load.[29]

ACKNOWLEDGMENTS

The authors would like to thank Joost van der Neut for his valuable input.

References

[1]N. K. Martiartu, C. Boehm, and A. Fichtner, "3d wave-equation-based finite-frequency tomography for ultrasound computed tomography," IEEE Transactions on Ultrasonics, Ferroelectrics, and Frequency Control (2020).

[2]R. J. Lavarello and M. L. Oelze, "Tomographic reconstruction of three-dimensional volumes using the distorted born iterative method," IEEE Transactions on Medical Imaging

28(10), 1643–1653 (2009).

[3]H. Gemmeke and N. Ruiter, "3d ultrasound computer tomography for medical imaging," Nuclear Instruments and Methods in Physics Research Section A: Accelerators, Spectrometers, Detectors and Associated Equipment **580**(2), 1057–1065 (2007).

[4]N. Ozmen, R. Dapp, M. Zapf, H. Gemmeke, N. V. Ruiter, and K. W. A. van Dongen, "Comparing different ultrasound imaging methods for breast cancer detection," IEEE Trans. Ultrason., Ferroelectr., Freq. Control **62**(4), 637–646 (2015).

[5]M. Pérez-Liva, J. Herraiz, J. Udías, E. Miller, B. Cox, and B. Treeby, "Time domain reconstruction of sound speed and attenuation in ultrasound computed tomography using full wave inversion," The Journal of the Acoustical Society of America **141**(3), 1595–1604 (2017).

[6]G. Y. S. Sandhu, C. Li, O. Roy, S. Schmidt, and N. Duric, "High-resolution quantitative whole-breast ultrasound: in vivo application using frequency-domain waveform tomography," in *Medical Imaging 2015: Ultrasonic Imaging and Tomography*, International Society for Optics and Photonics (2015), Vol. 9419, p. 94190D.

[7]K. Wang, T. Matthews, F. Anis, C. Li, N. Duric, and M. A. Anastasio, "Waveform inversion with source encoding for breast sound speed reconstruction in ultrasound computed tomography," IEEE transactions on ultrasonics, ferroelectrics, and frequency control **62**(3), 475–493 (2015).

[8]N. Duric, P. Littrup, L. Poulo, A. Babkin, R. Pevzner, E. Holsapple, O. Rama, and C. Glide, "Detection of breast cancer with ultrasound tomography: First results with the

computed ultrasound risk evaluation (cure) prototype," Medical physics **34**(2), 773–785 (2007).

[9]L. Guasch, O. C. Agudo, M.-X. Tang, P. Nachev, and M. Warner, "Full-waveform inversion imaging of the human brain," NPJ Digital Medicine **3**(1), 1–12 (2020).

[10]S. Bernard, V. Monteiller, D. Komatitsch, and P. Lasaygues, "Ultrasonic computed tomography based on full-waveform inversion for bone quantitative imaging," Physics in Medicine & Biology **62**(17), 7011 (2017).

[11]B. Malik, J. Klock, J. Wiskin, and M. Lenox, "Objective breast tissue image classification using quantitative transmission ultrasound tomography," Scientific reports **6**, 38857 (2016).

[12]X. Song, M. Li, F. Yang, S. Xu, and A. Abubakar, "Feasibility study of acoustic imaging for human thorax using an acoustic contrast source inversion algorithm," The Journal of the Acoustical Society of America **144**(5), 2782–2792 (2018).

[13]P. Mojabi and J. LoVetri, "Ultrasound tomography for simultaneous reconstruction of acoustic density, attenuation, and compressibility profiles," The Journal of the Acoustical Society of America **137**(4), 1813–1825 (2015).

[14]P. Mojabi and J. LoVetri, "Evaluation of balanced ultrasound breast imaging under three density profile assumptions," IEEE Transactions on Computational Imaging **3**(4), 864–875 (2017).

[15]K. W. A. van Dongen and W. M. Wright, "A full vectorial contrast source inversion scheme for three-dimensional acoustic imaging of both compressibility and density profiles," The

Journal of the Acoustical Society of America **121**(3), 1538–1549 (2007).

[16]U. Taskin, J. van der Neut, H. Gemmeke, and K. W. A. van Dongen, "Redatuming of 2-d wave fields measured on an arbitrary-shaped closed aperture," IEEE transactions on ultrasonics, ferroelectrics, and frequency control **67**(1), 173–179 (2019).

[17]A. De Hoop, "Handbook of radiation and scattering of waves: Acoustic waves in fluids, elastic waves in solids, electromagnetic waves: with corrections," Former publisher: Academic Press (2008).

[18]J. T. Fokkema and P. M. van den Berg, *Seismic applications of acoustic reciprocity* (Elsevier, 2013).

[19]F. B. Jensen, W. A. Kuperman, M. B. Porter, and H. Schmidt, *Computational ocean acoustics* (Springer Science & Business Media, 2011).

[20]M. Abramowitz, "Abramowitz and stegun: Handbook of mathematical functions," US Department of Commerce **10** (1972).

[21]A. B. Ramirez and K. W. A. van Dongen, "Sparsity constrained contrast source inversion," The Journal of the Acoustical Society of America **140**(3), 1749–1757 (2016).

[22]K. W. A. van Dongen and W. M. Wright, "A forward model and conjugate gradient inversion technique for low-frequency ultrasonic imaging," The Journal of the Acoustical Society of America **120**(4), 2086–2095 (2006).

[23]T. L. Szabo, *Diagnostic ultrasound imaging: inside out* (Academic Press, 2004).

[24]F. A. Duck, *Physical properties of tissues: a comprehensive reference book* (Academic press, 2013).

[25]U. Taskin, N. Ozmen, H. Gemmeke, and K. W. A. van Dongen, "Modeling breast ultrasound; on the applicability of commonly made approximations," Archives of Acoustics **43**(3) (2018).

[26]A. B. Ramirez, S. A. Abreo, and K. W. A. van Dongen, "Selecting the number and location of sources and receivers for non-linear time-domain inversion," in *2017 IEEE International Ultrasonics Symposium (IUS)*, IEEE (2017), pp. 1–3.

[27]P. M. van den Berg and A. Abubakar, "Contrast source inversion method: State of art," Progress in Electromagnetic Research **34**, 189–218 (2001).

[28]A. Abubakar and P. M. Van Den Berg, "Total variation as a multiplicative constraint for solving inverse problems," IEEE Transactions on Image Processing **10**(9), 1384–1392 (2001).

[29]U. Taskin and K. W. A. van Dongen, "3-d redatuming for breast ultrasound," in *Medical Imaging 2020: Physics of Medical Imaging*, International Society for Optics and Photonics (2020), Vol. 11312, p. 113125H.